Available online at www.sciencedirect.com
ScienceDirect
Journal of Power Sources 174 (2007) 501–507
JOURNAL OF POWER SOURCES
www.elsevier.com/locate/jpowsour

$FePO_4$ nanoparticles supported on mesoporous SBA-15: Interesting cathode materials for Li-ion cells

C. Gerbaldi [a,*], G. Meligrana [a], S. Bodoardo [a], A. Tuel [b], N. Penazzi [a]

[a] *Dipartimento di Scienza dei Materiali e Ingegneria Chimica, Politecnico di Torino, c.so Duca degli Abruzzi, 24, 10129 Torino (TO), Italy*
[b] *Institut de Recherches sur la Catalyse, CNRS (UPR 5401) 2 Avenue Albert Einstein, 69626 Villeurbanne Cedex, France*

Available online 30 June 2007

Abstract

Exploiting the properties of stability, low cost and low toxicity of iron phosphates, we have tried to enhance the performance of $FePO_4$ as cathode material for Li-ion cells. We adopted the strategy of obtaining $FePO_4$, via a typical preparation, onto the channels of an ordered mesoporous SBA-15 silica, a low cost mesoporous material commonly used in industry, which possesses larger pores, thicker walls and higher thermal stability as compared with other mesoporous silicas like MCM-41. Characterizations with ICP-AES, XRPD, BET and HRTEM suggest that the supported iron phosphate species, with loading amounts as high as 30 wt%, are located and dispersed in the mesopores of SBA-15. Iron phosphate can be reduced/oxidized more readily than the unsupported iron phosphate at room temperature, and in fact, cycling at *C*/10, the supported phosphate shows a utilization of 70% with respect to a value of 30% for the unsupported solid. The result is interesting from the scientific viewpoint but not suitable for application at the moment. Indeed, the amount of active material does not exceed 30% of the electrode mass and the total electrode capacity, though the active material is very efficient, is largely insufficient. Researches are being developed trying to increase the performances of the materials and also to eliminate the support after the dispersion of the active material.

Keywords: Li-ion batteries; Mesoporous; Iron(III) phosphate; Wet Impregnation; Electrochemical tests

1. Introduction

Innovative fields of application for Li-ion batteries, like the electric vehicle (EV) technology, put in particular evidence the importance, for the electrode materials, of being ecologically friendly and low cost. Moreover, the cell voltage seems no longer of primary importance: high voltage is desirable, but it is in general related to the instability of the material and to possible problems with the electrolyte. High performance at ambient temperature is also not so important as one deals with temperatures of 60–80 °C in EV applications.

Recently, the whole of these considerations raised the interest for Fe(III) stable phosphates, particularly $FePO_4$. Its Fe^{3+}/Fe^{2+} couple potential (about 3.0 V versus Li^+/Li) is not so high to arise problems of stability of the system, and not so low to give an insufficient specific power. The theoretical capacity is high: 178 mAh g^{-1} for the anhydrous form (for the well known phospho-olivine $LiFePO_4$ it is 170 mAh g^{-1}), and 143 mAh g^{-1} for $FePO_4{\cdot}2H_2O$. Moreover, the synthesis of a Fe(III) compound, due to the Fe(III) stability, is less critical as compared to Fe(II) materials. Nevertheless, the behavior of $FePO_4$ cathode materials suffers from a difficult diffusion of Li^+ ions inside the structure and from a very low electronic conductivity.

Thus, improvement of the electrochemical behavior has followed different lines in time. Most of researchers have focused their interest on the possible $FePO_4$ structures (crystalline or amorphous, anhydrous or with constitutional water) searching for the particular one capable of promoting the electrochemical properties. According to the first investigations [1–3], the hydrated amorphous $FePO_4$ shows a superior electrochemical performance, due to the faster ionic diffusion promoted by the hydration water [1]. Prosini et al. succeeded in measuring the diffusion coefficient for amorphous $FePO_4{\cdot}1.5H_2O$, the very low value was related to the low electronic conductivity of the material [3]. The electrode did not show a high specific capacity, but the good rechargeability was related to its amorphous character.

* Corresponding author. Tel.: +39 011 564 46 38; fax: +39 011 564 46 99.
E-mail address: claudio.gerbaldi@polito.it (C. Gerbaldi).

0378-7753/$ – see front matter © 2007 Elsevier B.V. All rights reserved.
doi:10.1016/j.jpowsour.2007.06.176

Zaghib and Julien [4] studied monoclinic $FePO_4 \cdot 2H_2O$ finding specific capacity values similar as in Ref. [3]. They limited the investigation to the first cycle but IR spectra of the discharged electrode gave evidence of structural modifications due to the Li^+ insertion and reduction of Fe^{3+} ions. Okada et al. [5] studied a low cost preparation to obtain amorphous or crystalline hydrated $FePO_4$; the performance was very good, but the rechargeability of the crystalline was worse than the amorphous samples. In their experiments, Croce et al. [6] considered the anhydrous α-quartz $FePO_4$ polymorph, an electrochemically inert structure [1,4], and improved its poor electronic conductivity by adding ascorbic acid during synthesis so that its decomposition to finely divided carbon during annealing could promote the electronic contact between the $FePO_4$ particles. The morphology of the electrode was optimized by a ball milling stage in presence of SuperP carbon. Nonetheless, to reach satisfactory results, it was necessary to add also low size particles of RuO_2 during the preparation aiming at obtaining effective intra-$FePO_4$ particle contact.

Guo et al. [7] and, later, Shi et al. [8] modified the morphology of the phosphate making it mesostructured. An open structure is obtained with a high surface area, easily accessible by the Li^+ ions from the electrolyte. Moreover, the bulk zones, i.e. the pore walls, which hinder the electronic conductivity, are of limited extent. All these characteristics strongly improve $FePO_4$ electrochemical performances. Guo did not report electrochemical data; moreover, the synthesis implied the use of HF and appeared problematic from an ecological viewpoint. Shi et al. [8], starting from a modified template method, obtained amorphous but mesoporous $FePO_4$ to be used as cathode active material. The best results corresponded to the conditions leading to the highest specific surface area and residual carbon percentage, which again here, helps conductivity.

Our investigations on this subject aimed at obtaining an iron phosphate with good electrochemical performances as those allowed by the mesostructured morphology, but prepared by a simple and inexpensive process. Therefore, we adopted the strategy of preparing $FePO_4$ inside the channels of an ordered mesoporous SBA-15 silica, a commonly used in industry low cost mesoporous material, which possesses larger pores, thicker walls and higher thermal stability as compared with other mesoporous silicas (e.g. MCM-41, MCM-48) [9]. Instead of using a commercial mesoporous material, we prepared the mesoporous support as well, following a procedure that allows to cover the interior surface of the mesopores with a carbon film, so promoting the electronic conductivity among the phosphate particles. The results of our first experiments are reported in the present paper.

2. Experimental

2.1. Synthesis

Mesoporous SBA-15 silica has been synthesized, following a variation of the procedures described in the literature [9–11], using tetraethyl orthosilicate (Aldrich, TEOS), Pluronic P123 triblock co-polymers (Aldrich, EO_{20}-PO_{70}-EO_{20}), hydrochloric acid (Fluka, HCl 37 wt%) and doubly distilled water as reactants.

In a typical preparation, after stirring the reactants for 20 h at 40 °C, the resulting white-gel solution is transferred into a Teflon bottle and statically heated at 100 °C for 24 h. After being cooled to room temperature, the solid white product is recovered by filtering, washed several times with doubly distilled water, and air-dried at room temperature overnight. Yields are ∼95% (based on silicon), which is comparable to the syntheses described in the literature [9,11–13]. The surfactant-containing SBA-15 powder is pre-heated at 200 °C for 2 h and then, treated at 515 °C for 10 h under flowing N_2, in order to decompose the block co-polymer surfactant and produce a carbon layer which covers the surface of the mesopores, so enhancing the electronic conductivity, as already reported by Zhu et al. [14]. After this process, the sample changes from the original white (as-synthesized SBA-15) to brown. This change in color is an evidence of successful lodging of carbon on the surface of the SBA-15.

$FePO_4$ is introduced into the mesopores of SBA-15 by the wetness impregnation method. In a typical preparation, approximately 1.0 g of N_2-calcined SBA-15 is immersed into a mixed solution of $Fe(NO_3)_3 \cdot 9H_2O$ and $NH_4H_2PO_4$ (Fe/P = 1) and it is allowed to stir for 12 h at room temperature. The slurry is then dried at 75 °C with continuous stirring. The dried powder is finally heat-treated for 8 h at 515 °C (heating ramp 2.0 °C min^{-1}) under flowing N_2.

Two SBA-15 supported samples have been prepared by this procedure, with different loading amounts of $FePO_4$ (namely 15 and 30 wt%, respectively).

2.2. Chemical, structural analysis and characterization

Quantitative elemental analysis has been carried out by inductively coupled plasma–atomic emission spectroscopy (ICP-AES) with a Varian Liberty 100 instrument. The samples have been digested in hot concentrated $HCl:HNO_3 = 3:1$ mixture.

The X-ray diffraction profiles of the samples have been obtained using a Philips Xpert MPD powder diffractometer, equipped with Cu Kα radiation ($V = 40$ kV, $i = 30$ mA) and a curved graphite secondary monochromator. The diffraction profiles have been collected in the 2θ range between 0.5° and 5° for the low diffraction angles patterns and between 10° and 60° for the high diffraction angles patterns, both with an acquisition step of 0.02° and a time per step of 10 s.

The samples have also been submitted to a high-resolution transmission electron microscope (HRTEM) investigation for the morphological characterization, using a JEOL 2010 microscope with an accelerating voltage of 200 kV.

Specific surface areas (SSA) have been determined using the Brunauer, Emmet, Teller (BET) method on an ASAP 2010 Micromeritics instrument. Prior to adsorption, approximately 50.0 mg of solid have been placed in the cell and evacuated at 350 °C for 5 h. The pore diameter distribution has been evaluated by the Barrett–Joyner–Halenda (BJH) method with the corrected form of the Kelvin equation.

2.3. Electrochemical testing

The electrodes for the evaluation of the electrochemical properties have been prepared by spreading on an aluminum current-collector, following the so-called "doctor blade" technique, a slurry of the active material (70 wt%) with acetylene black (Shawinigan Black AB50, Chevron Corp., USA.) as electronic conductor (20 wt%) and poly(vinylidene fluoride) (PVdF, Solvay Solef 6020) as binder (10 wt%) in *N*-methyl-2-pyrrolidone (NMP, Aldrich). After the evaporation of the solvent by a mild heating, disks of 0.785 cm^2 are punched out of the foil and dried by heating them at about 130 °C under high vacuum for 5 h. After their transfer in an Ar-filled dry glove box, the disks are weighed before their use in the test cells and, by subtraction of the average weight of the Al disks, the weight of the coating mixture is calculated. The composite electrodes are used in three electrodes T-cells with lithium metal (high purity lithium foils, Merck) as both the counter and the reference electrodes and two glass-wool (Whatman GF/A) discs as the separator.

The evaluation of the electrochemical performances as cathodes for Li-ion cells has been carried out by galvanostatic discharge/charge cycling and cyclic voltammetry at room temperature with an Arbin Instrument Testing System model BT-2000.

3. Results and discussion

3.1. Chemical analysis

The results of the ICP-AES elemental analysis are reported in Table 1, showing that for both the samples prepared, the expected $FePO_4$ stoichiometry (Fe:P = 1:1) has been obtained.

3.2. Structural and morphological results

The small-angle XRPD patterns for as-synthesized and N_2-calcined mesoporous SBA-15 silica are reported in Fig. 1.

Both materials show the typical features of mesoporous SBA-15 silica [9,14–16]. The as-synthesized sample (dash line) shows three well-resolved peaks at $2\theta = 0.88$, 1.50 and 1.71, respectively, that are indexable as (1 0 0), (1 1 0) and (2 0 0) reflections associated with *p6mm* hexagonal symmetry. The four additional weak peaks in the 2θ range between 2.0° and 3.5° correspond to the (2 1 0), (3 0 0), (2 2 0), and (3 1 0) scattering reflections, indicating that the SBA-15 has a high degree of hexagonal mesoscopic organization. The intense (1 0 0) peak reflects a *d* spacing of 100.4 Å.

In consequence of the heat-treatment in N_2 at 515 °C for 10 h, the XRPD pattern (see Fig. 1, solid line) shows that the *p6mm* morphology is preserved, although the diffraction peaks appear at slightly larger 2θ values, with $d_{100} = 95.0$ Å and $a_0 = 109.7$ Å. Six XRPD peaks are still observed, confirming that the hexagonal SBA-15 is high thermally stable and illustrating that the presence of carbon did not influence the mesoscopic organization. The increase in peaks intensity after calcination is due to the greater scattering density contrast and reduced X-ray absorbance after surfactant and polymer decomposition [17].

Table 1
ICP-AES analysis on SBA-15 supported $FePO_4$ samples

Sample	Fe (wt%)	P (wt%)
15 wt% $FePO_4$/SBA-15	5.42	3.01
30 wt% $FePO_4$/SBA-15	11.17	6.18

The values are expressed in wt% of total weight.

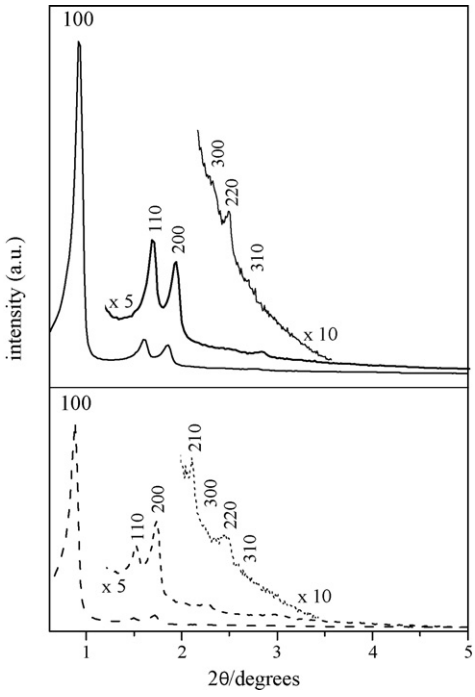

Fig. 1. X-ray powder diffraction patterns of (dash line) as-synthesized and (solid line) N_2-calcined mesoporous SBA-15 silica. Low diffraction angles pattern, $0.5° < 2\theta < 5°$.

The loading of $FePO_4$ onto the mesopores of N_2-calcined SBA-15 leads to a decrease in the intensity of the diffraction lines and a slight shift of the diffraction peaks to higher 2θ values, as

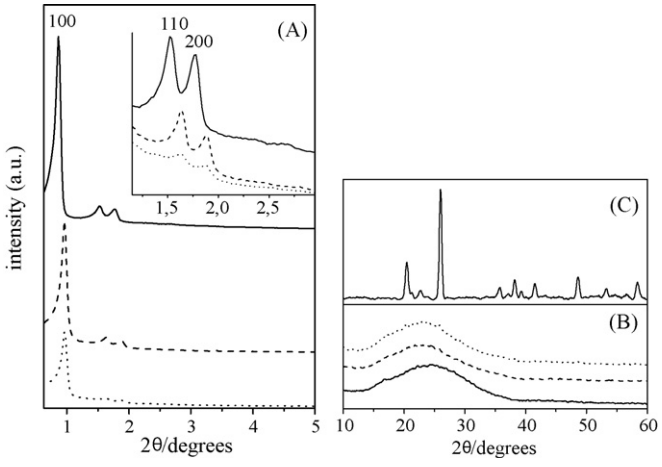

Fig. 2. X-ray powder diffraction patterns of (solid line) N_2-calcined pristine SBA-15, (dash line) SBA-15 supported 15 wt% $FePO_4$, (dot line) SBA-15 supported 30 wt% $FePO_4$. (A) Low diffraction angles pattern, $0.5° < 2\theta < 5°$, (B) high diffraction angles pattern, $10° < 2\theta < 60°$ and (C) unsupported $FePO_4$.

Table 2
Comparative table of results from XRPD and N_2 sorption experiments

Sample	N_2-calc. SBA-15	SBA-15 $FePO_4$ 15 wt%	SBA-15 $FePO_4$ 30 wt%
d_{100} (Å)	95.0	91.6	91.0
a_0(Å)	109.7	105.8	105.0
SSA ($m^2\,g^{-1}$)	889.3	548.6	459.2
Desorption pore diameter (Å)	67.3	53.2	52.6

shown in Fig. 2A, that presents the X-ray powder diffraction patterns of the SBA-15 supported $FePO_4$ materials in comparison with the unsupported N_2-calcined SBA-15.

The intensity decrease becomes much more notable when the loading amount of guest compound reaches 30 wt% (dot line of Fig. 2A). As it is clearly evidenced by HR-TEM pictures (see Fig. 4), the decrease of XRPD intensities cannot be attributed to a loss of long-range hexagonal structure upon impregnation with $FePO_4$, but most likely to a change in the scattering density contrast. All the characteristics of pristine SBA-15, in particular a high mesoporous order, are well maintained even after a 30 wt% $FePO_4$ loading.

The (1 0 0) Bragg reflections can be indexed with a hexagonal unit cell: $a_0 = 109.7$ Å ($a_0 = 2d_{100}/\sqrt{3}$) for N_2-calcined SBA-15, $a_0 = 105.8$ Å for $FePO_4$ (15 wt%)-SBA-15, and $a_0 = 105.0$ Å for $FePO_4$ (30 wt%)-SBA-15, respectively (see Table 2). The near retention of the unit cell indicates that the structure is maintained upon the loading of high amounts of $FePO_4$, confirming the high stability of SBA-15.

The X-ray powder diffraction patterns at higher angles ($2\theta = 10$–60°) are shown in Fig. 2B. No reflections of crystalline $FePO_4$ phases can be detected, but only the broad reflection of the amorphous wall-structure of the SBA-15. No crystalline phase appears even when the loading amount reaches 30 wt%, showing that $FePO_4$ is probably amorphous, or the scattering domains are so small that the large line width of the reflections makes it impossible to discern them from the background. These results allow to consider that the $FePO_4$ species are most likely located inside the mesopores, dispersed on the wall surface of SBA-15 channels.

To have a confirmation that only iron(III) phosphate is formed onto the pores of SBA-15 under these experimental conditions, a mixed solution of $Fe(NO_3)_3{\cdot}9H_2O$ and $NH_4H_2PO_4$ (Fe/P = 1) has been prepared and treated in the same way as for the wetness impregnation of SBA-15. The brown crystalline powder obtained after the heating treatment has been identified as trigonal $FePO_4$ (s.g. P321) by means of X-ray powder diffraction (see Fig. 2C). The unsupported $FePO_4$ is mainly composed of a quartz-like phase as well as of a small amount of tridymite-like phase.

Representative N_2 adsorption/desorption isotherms at 77 K are shown in Fig. 3 for N_2-calcined SBA-15 and the SBA-15 supported $FePO_4$ samples, calcined at 515 °C in flowing N_2.

The result for N_2-calcined SBA-15 (squares) matches very well with those reported in the literature and presents a type-IV isotherm (IUPAC classification [18]), as it is expected for mesoporous systems [19]. Three well-distinguished regions of the adsorption isotherm are evident: a monolayer-multilayer adsorption, a capillary condensation, and a multilayer adsorption on the outer particles surface. A clear H_1-type hysteresis loop is observed, which is typical of mesoporous materials with one-dimensional cylindrical channels [9,12], and the capillary condensation occurs at a $p/p_0 = 0.65$–0.75. The sharp inflection in this isotherm corresponds to capillary condensation within uniform mesopores, reflecting the uniform pore size in this material.

The characteristics of the isotherm for the SBA-15 supported with 15 wt% $FePO_4$ (circles in Fig. 3) is similar to the one obtained for the unsupported material. The amount of physisorbed gas is reduced, due to a smaller specific surface. The sharp inflection due to capillary condensation is slightly shifted towards lower pressure values, indicating a smaller pore size. The sharpness of this step reflects the uniform pore size in this material. The amount of physisorbed nitrogen further decreases

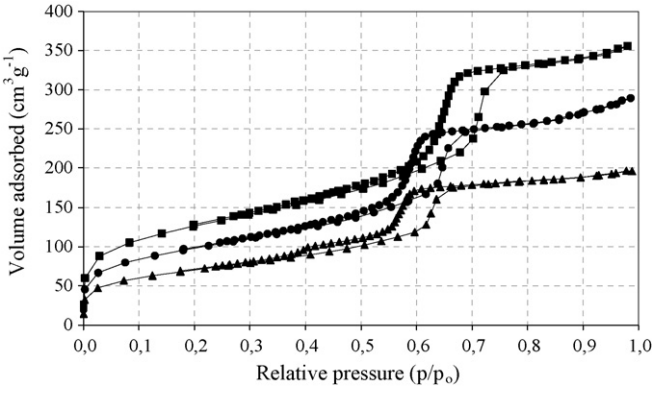

Fig. 3. Adsorption/desorption isotherms of N_2 at 77 K on N_2-calcined SBA-15 (squares), $FePO_4$ (15 wt%)-SBA-15 (circles) and $FePO_4$ (30 wt%)-SBA-15 (triangles), calcined at 515 °C in flowing nitrogen.

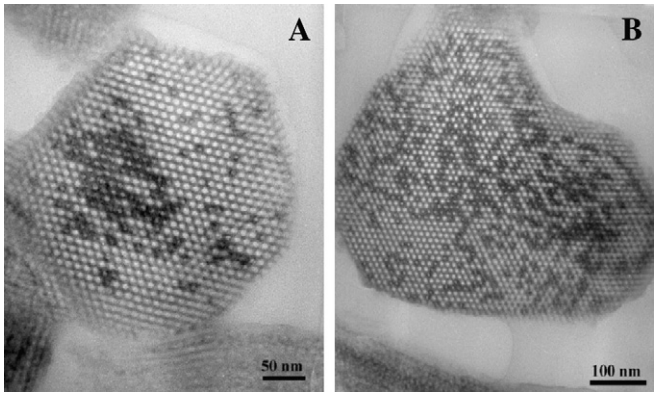

Fig. 4. HR-TEM images of (A) 15 wt% $FePO_4$/SBA-15 and (B) 30 wt% $FePO_4$/SBA-15, taken with the beam parallel to the pore direction.

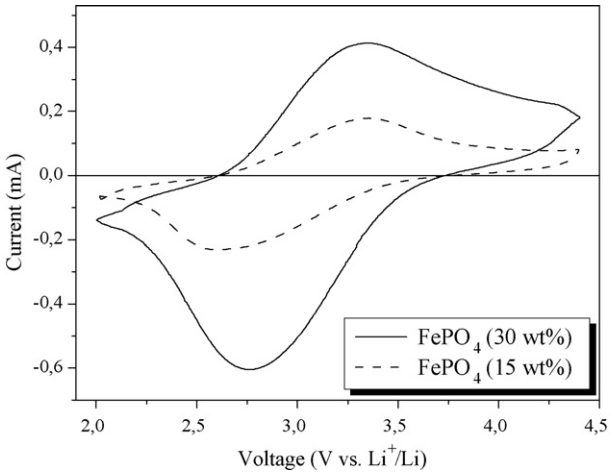

Fig. 5. Second voltammetric cycle for the SBA-15 supported $FePO_4$ samples: scan rate = 0.100 mV s^{-1} and voltage range = 2.0–4.4 V vs. Li^+/Li.

when increasing the loading amount of $FePO_4$ to 30 wt% (triangles in Fig. 3), accompanied with a shift of the inflection point of the step to smaller p/p_0 values. The reduced amount of physisorbed N_2 is caused by a further decrease of the specific surface area, while the occurrence of the step at slightly lower relative pressure is indicative of even smaller pore sizes.

Furthermore, a second inflection point at $p/p_0 \approx 0.4$ is characteristic of intracrystalline voids, probably formed by local dissolution of silica during the impregnation. However, reversible adsorption/desorption of nitrogen is observed for both the SBA-15 supported $FePO_4$ samples. These facts indicate that there is negligible obstruction of the pores, as already reported by other authors [20,21].

Table 2 summarizes the porous properties of synthesized materials determined from X-ray powder diffraction and N_2 physisorption measurements at 77 K. A mean pore size of 67.3 Å, calculated on the desorption branch of the isotherm according to the standard Barrett–Joyner–Halenda (BJH) method with the corrected form of the Kelvin equation, and a BET specific surface area of 889.3 m^2 g^{-1} are obtained from the isotherm of N_2-calcined SBA-15. BET surface area and pore volume decrease with increasing the loading amount of $FePO_4$ species on the pore walls of SBA-15. The reduction in size is especially reflected in the BET surface area, which shows a reduction of about 38%, in consequence of the loading of 15 wt% of $FePO_4$. The observation of the decreased surface area may be an indication of the formation of $FePO_4$ nanoclusters within the mesopores. The pore diameter (Table 2) changes in the same way: 21% pore size decrease for the 15 wt% sample and practically the same decrease for the 30 wt%. The wall thickness increases from ca. 42 to 52 Å upon loading with 30 wt% $FePO_4$. Note that $FePO_4$ itself exhibits a very low surface area of 3.3 m^2 g^{-1}.

Representative high-resolution transmission electron microscopy (HR-TEM) images of the SBA-15 supported $FePO_4$ materials, taken with the beam parallel to the pore direction, are reported in Fig. 4.

They show well-ordered hexagonal arrays of mesopores and further indicate that SBA-15 has a two-dimensional *p6mm* hexagonal structure [9,15,16]. The (1 0 0) direction retains a regular hexagonal array of uniform channels characteristic of mesoporous SBA-15. Each pore is surrounded by six neighbors and its hexagonal structure is unaffected by the presence of $FePO_4$. The d_{100} value and the diameter of the channels as obtained from transmission electron microscopy well correspond to the d_{100} values calculated from the X-ray powder diffraction pattern. However, it is not possible to observe directly the presence of carbon films from the TEM images, probably because the coating layer is too thin to be detected.

HR-TEM observations confirm the previous experimental results and further support the encapsulation of $FePO_4$ nanoparticles within the SBA-15 mesopores, even if the dispersion of the species is not fully homogeneous. Small clusters encapsulated inside the mesoporous channels can be discerned. No large particles located outside the mesopores are observed even for the 30 wt% $FePO_4$ sample (Fig. 4B), which is a further confirmation that iron phosphate is exclusively formed within the pore system. All other images recorded have been found to be similar, within and between the samples.

3.3. Electrochemical results as cathodes in lithium cells

The electrochemical behavior of the synthesized SBA-15-supported $FePO_4$ samples as cathodes for Li-ion batteries has been tested via cyclic voltammetry and galvanostatic charge/discharge cycles. Cyclic voltammetries (CVs) have been carried out at room temperature in three electrode T-cells with lithium metal as both the counter and the reference electrode. The potential ranged between 2.00 and 4.40 V versus Li^+/Li with a scan rate of 0.100 mV s^{-1}. The scanning begins towards the decreasing potential branch, choosing as starting value the V_{OC} of the cell. The galvanostatic discharge–charge cycling tests have been performed at room temperature in three electrode T-cells with lithium metal as the anode, setting the cut-off voltages to 2.00–4.00 V versus Li^+/Li. The liquid electrolyte used has been 1.0 M $LiPF_6$ in a 1:1 mixture of ethylene carbonate (EC) and diethyl carbonate (DEC).

The second voltammetric cycles for the SBA-15 supported 15 and 30 wt% $FePO_4$ samples are reported in Fig. 5.

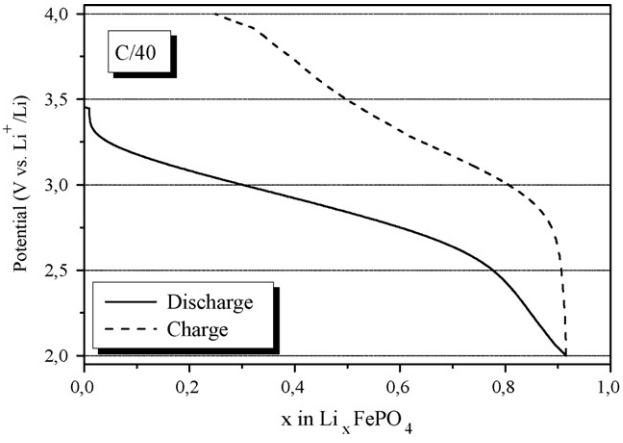

Fig. 6. First discharge/charge profiles at *C*/40 rate of the SBA-15 supported 30 wt% $FePO_4$ sample at room temperature.

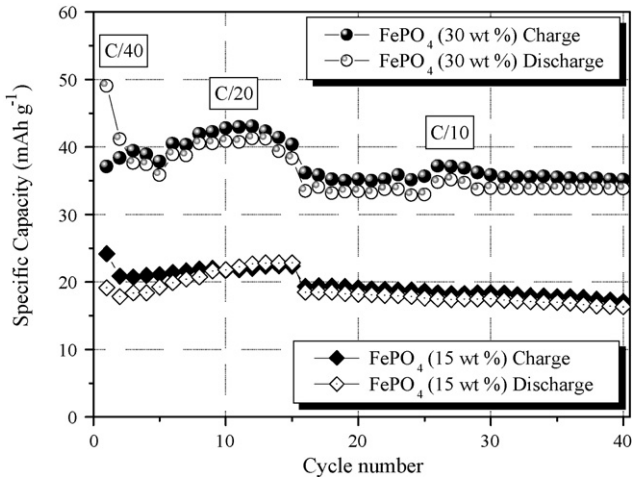

Fig. 7. Cycling performance of the SBA-15 supported $FePO_4$ samples at room temperature, cycled at different *C*-rates ranging from *C*/40 to *C*/10 with respect to a theoretical specific capacity of 178 mAh g^{-1} for $FePO_4$ (corresponding to a calculated electrode specific capacity of 54 mAh g^{-1} for the $FePO_4$ 30 wt% and 27 mAh g^{-1} for the $FePO_4$ 15 wt% composite electrode).

The couples of peaks in the two voltammograms are both centered at a mid-point potential of approximately 3.05 V versus Li^+/Li, ascribable to the Fe(III)/Fe(II) redox couple. As expected, the intensity of the peaks for the 15 wt% $FePO_4$ sample is lower with respect to the 30 wt% one. Last, the presence of a single couple of peaks per voltammogram indicates that there are no other electrochemically active species in the range of potentials chosen.

The experimental results point out that the iron(III) phosphate nanoparticles loaded inside the mesoporous structure are electrochemically active to the Li^+ ion insertion/de-insertion, and that the process is almost reversible, as roughly evidenced by the intensity of the reduction peaks, slightly higher than that of the oxidation ones.

The cycling behavior of the samples at room temperature is presented in Figs. 6 and 7. The cycling tests consisted of a galvanostatic discharge/charge at *C*/40 rate for the first cycle, then at *C*/20 for a period of 14 cycles and, finally, at *C*/10 for a period of 25 cycles. The first discharge/charge cycle has been carried out at low *C*/40 rate, as it has been experimentally observed that the obtained specific capacity is higher if the electrode is activated by performing a first cycle at slow *C*-rate. The *C*-rate values used in these preliminary tests are quite low, as we have experienced stability problems of the impregnated $FePO_4$ during the first tests.

Fig. 6 shows the initial discharge and charge profiles of the SBA-15 supported 30 wt% $FePO_4$ sample cycled at *C*/40 rate in the voltage range of 4.0–2.0 V versus Li^+/Li. The behavior is similar to what is reported in the literature about $FePO_4$ [1–5]. The curves have the characteristic S-type shape centered at an average voltage of about 3 V versus Li^+/Li for the Fe(III)/Fe(II) redox couple. The sample shows a quite high difference of the potential values between the discharge and the charge profiles, ascribable not only to the reaction over-potential but to some initial phenomenon, perhaps a $FePO_4$ surface modification, hindering the transfer of the Li^+ ions. As evidenced in Fig. 7, this behavior, only found in the 30 wt% sample, ceases after the first cycle and the following ones show a good cycling retention and a slight dependence, at least at these low regimes, from the *C*-rate.

Of course, due to the low percentage of active material, the electrode capacity is very low, corresponding to a total energy density unsuitable for any application, at the moment.

But, if we refer to the active material only, then we find a very high utilization coefficient: about 70% of the total specific capacity at *C*/10, similar to the best results obtained in the literature with samples undergone particular treatments. It is important to note that a $FePO_4$ cathode, prepared by the same process used during impregnation, but not supported, gave only 40% of the theoretical capacity at *C*/10 rate.

4. Conclusions

Two amounts of $FePO_4$ (15 and 30 wt%) have been loaded inside the channels of ordered mesoporous SBA-15 silica leading to an interesting material as cathode for Li-ion cells.

The impregnation procedure with $FePO_4$ is very simple, with no critical parameters. The mesoporous material used is common and well known. The iron phosphate species are located exclusively inside the mesopores of SBA-15, forming small clusters when the loading amount is as high as 30 wt%.

The preliminary results obtained on the electrodes performance, though clearly unsatisfying from the applicative point of view (very low specific capacities), are nonetheless interesting from the scientific viewpoint because of the high utilization coefficient values. The important finding is that no matter what the $FePO_4$ structure be, its dispersion into the pores of an open-structure mesoporous material, like SBA-15, enhances the electrochemical performances. Important is also the presence of a conductive layer of carbon inside the SBA-15 pore walls. This point is worth a thorough investigation in future.

There are different ways of enhancing the electrochemical performances of the electrode to an application level, all of them actually followed by our research group. Major efforts will be directed to increase the percentage of $FePO_4$ lodged onto the pores. In addition, one can choose an equally economical mesoporous material having pores on the three spatial directions, e.g. MCM-48 or KIT-16. Finally, $FePO_4$ nanorods can be obtained (and virtually get an $FePO_4$ only electrode) by eliminating the mesoporous substrate after impregnation.

Acknowledgement

The authors wish to thank the Italian Regione Piemonte Administration for supporting the costs of the present research.

References

[1] C. Masquelier, P. Reale, C. Wurm, M. Morcrette, L. Dupont, D. Larcher, J. Electrochem. Soc. 149 (2002) A1037.
[2] Y. Song, S. Yang, P.Y. Zavalij, M.S. Whittigham, Mater. Res. Bull. 37 (2002) 1249.
[3] P.P. Prosini, M. Lisi, S. Scaccia, M. Carewska, F. Cardellini, M. Pasquali, J. Electrochem. Soc. 149 (2002) A297.
[4] K. Zaghib, C.M. Julien, J. Power Sources 142 (2005) 279.

[5] S. Okada, T. Yamamoto, Y. Okazaki, J.-I. Yamaki, M. Tokunaga, T. Nishida, J. Power Sources 146 (2005) 570.
[6] F. Croce, A. D'Epifanio, P. Reale, L. Settimi, B. Scrosati, J. Electrochem. Soc. 150 (2003) A576.
[7] X. Guo, W. Ding, X. Wang, O. Yan, Chem. Commun. (2001) 709.
[8] Z. Shi, I. Li, W. Ye, Y. Yang, Electrochem. Solid State Lett. 8 (2005) A396.
[9] D. Zhao, J. Feng, Q. Huo, N. Melosh, G.H. Fredrickson, B.F. Chmelka, G.D. Stucky, Science 279 (1998) 548.
[10] W. Yang, X. Wang, Q. Guo, Q. Zhang, Y. Wang, New J. Chem. 27 (2003) 1301.
[11] Y. Wang, X. Wang, Z. Su, Q. Guo, Q. Tang, Q. Zhang, H. Wan, Catal. Today 93–95 (2004) 155.
[12] D. Zhao, J. Sun, Q. Li, G.D. Stucky, Chem. Mater. 12 (2000) 275.
[13] D. Zhao, Q. Huo, J. Feng, B.F. Chmelka, G.D. Stucky, J. Am. Chem. Soc. 120 (1998) 6024.
[14] S. Zhu, H. Zhou, M. Hibino, I. Honma, M. Ichihara, Mater. Chem. Phys. 88 (2004) 202.
[15] C.T. Kresge, M.E. Leonowicz, W.J. Roth, J.C. Vartuli, J.S. Beck, Nature 359 (1992) 710.
[16] Q. Huo, D.I. Margolese, G.D. Stucky, Chem. Mater. 8 (1996) 1147.
[17] P.J. Bruinsma, A.Y. Kim, J. Liu, S. Baskaran, Chem. Mater. 9 (1997) 2507.
[18] K.S.W. Sing, D.H. Everett, R.H.W. Haul, L. Moscou, R.A. Pierotti, J. Rouquerol, T. Siemieniewska, Pure Appl. Chem. 57 (1985) 603.
[19] R. Köhn, M. Fröba, Catal. Today 68 (2001) 227.
[20] S. Gómez, O. Giraldo, L.J. Garcés, J. Villegas, S.L. Suib, Chem. Mater. 16 (2004) 2411.
[21] H. Yang, G. Vovk, N. Coombs, I. Sokolov, G.A. Ozin, J. Mater. Chem. 8 (1998) 743.